Auton Robot (2011) 30: 427–443
DOI 10.1007/s10514-011-9227-2

Adaptive walking pattern generation and balance control of the passenger-carrying biped robot, HUBO FX-1, for variable passenger weights

Jung-Hoon Kim · Jung-Yup Kim · Jun-Ho Oh

Received: 3 May 2010 / Accepted: 7 March 2011 / Published online: 17 March 2011

Abstract A passenger-carrying biped robot is a practical robot capable of carrying a passenger for both entertainment purposes and disabled transport by means of biped walking. In the walking controls of the biped walking robot, changes in the payload are not generally considered. However, in the case of a passenger-carrying biped robot, the range of possible payloads for passenger weight is relatively wide, from zero to approximately one hundred kgf. In the authors' previous research pertaining to passenger-carrying biped robots, the robot was modeled using a specific passenger weight; hence, the control parameters were tuned for it and kept to be constant. However, the previous method's weakness was a decrease in the walking performance and walking stability of the robot when the passenger's weight was much heavier or lighter than the predefined passenger weight. Therefore, in this paper, the walking pattern generation and balance control methods are developed to adaptively cope with variable passenger weights. These methods are then experimentally verified to ensure that the walking performance could be preserved uniformly for a variation of passenger weights.

Keywords Passenger-carrying · Biped robot · Walking pattern generation · Balance control · Variable passenger weight

J.-H. Kim
Construction Robot and Automation Laboratory, Department of Civil and Environmental Engineering, Yonsei University, 134, Shinchon-dong, Seodaemun-gu, Seoul, 120-749, South Korea
e-mail: junghoon@yonsei.ac.kr

J.-Y. Kim (✉)
Humanoid Robot Research Laboratory, School of Mechanical Design & Automation Engineering, Seoul National University of Science and Technology, Gongrung-Dong, Nowon-Gu, Seoul, 139-743, South Korea
e-mail: jyk76@seoultech.ac.kr

J.-H. Oh
HUBO Laboratory, Humanoid Robot Research Center, Department of Mechanical Engineering, Korea Advanced Institute of Science and Technology, 373-1, Guseong-dong, Yuseong-gu, Daejeon, 305-701, South Korea
e-mail: jhoh@kaist.ac.kr

1 Introduction

Recently, many research groups have successfully developed life-size humanoid robots capable of walking in a human environment (Hirai et al. 1998; Akachi et al. 2005; Park et al. 2005; Ogura et al. 2006; Löffler et al. 2003). After successfully solving the problem of biped locomotion, many researchers have expanded the application field of human everyday life by applying various robotic technologies to the developed humanoid platform, including navigation, manipulation, and human robot interaction (Stilman et al. 2007; Gienger et al. 2005). As humanoid robotics is a future-oriented research field, the practical benefits of most applications are relatively few, and the level of technology required for development is relatively high. However, the passenger-carrying biped robot referenced in this paper is a practical biped robot capable of carrying a human. This robot is differentiated from the wheel-based type of vehicle, and it can be used in the welfare field as a walking wheelchair or a walking support machine that is able to the traverse stairs (Sugahara et al. 2004) and in the entertainment field as an amusing vehicle. In addition, previous research has considered this type of robot as having the potential to offer much greater mobility than that of a wheelchair (Chestnutt et al. 2006). The WL-16 (Waseda

Leg—No. 16) developed in 2003 was the world's first biped-walking robot capable of carrying a human (Sugahara et al. 2004). Its expected use was that of a multi-purpose locomotion vehicle. By designing a leg with a 6-DOF parallel mechanism, the mechanical rigidity was increased and the weight of the structural components was decreased. The weight of this original robot was 56 kgf, including the battery, and the height was approximately 1.2 m. Toyota released their "i-foot" robot in 2004, which was able to climb up and down staircases (Toyota motor corporation 2004). This machine was composed of serially connected rotary actuators, similar to that of the general humanoid robot, and the legs were bent toward the rear so that the passenger could ride comfortably on the robot. The height of the "i-foot" was 2.36 m, with a weight of 200 kgf. The maximum weight capacity of the passenger was 60 kgf, and the walking speed was 1.35 km/h. Subsequently, the HUBO FX-1 was first demonstrated to the public at the 2005 APEC summit, and the initial version of the control algorithm was published first in reference (Kim et al. 2007). This robot was designed for a maximum passenger weight of 100 kgf. Our previous paper (Kim et al. 2007) described the design of the passenger-carrying biped robot and the structural vibration control of the swing leg, which is different from that of a life-size humanoid robot, as well as the experiments performed for a passenger weight of 81 kgf. Passenger-carrying biped robots are different from the general life-size humanoid robots, such as ASIMO, HRP, and HUBO, in that these have their passenger seats on the lower limbs of the humanoids and the unknown passenger weight is applied as an additional payload. Therefore, the mechanism for increasing the rigidity of the lower limb structure needed to be designed (Sugahara et al. 2004) and the process for solving the structural vibration problem resulting from the weight reduction and its experimental verification was investigated (Kim et al. 2007). In the reference (Kim et al. 2007), all of the parameters for the walking patterns and online controllers were tuned for a specific passenger weight of 81 kgf. In the passenger-carrying biped robots on which passengers are able to have a variety of weights, from lighter children to heavier adults, it is very important that the walking performance does not change with passenger weight. In order to realize this objective, the walking pattern generation and online feedback controllers for biped walking must have adaptive characteristics that enable the parameters to be suitably determined for each of the variable passenger weights. Therefore, by focusing on the variable mass, which has not been covered in previous research, this paper describes the novel walking pattern generator and controllers that have been designed for variable masses.

This paper is organized as follows. In Sect. 2, we briefly describe the design specifications, sensors, and mechanical and electrical hardware of the passenger-carrying biped robot HUBO FX-1. In Sect. 3, we introduce the walking pattern generation method using the convolution sum. Since this method contains the analytic function of variable mass, it can effectively calculate the walking pattern for variable passenger masses. In this section, we also detail the variations in walking pattern with passenger weight. In Sect. 4, we address the balance controllers that perform the real-time feedback control using the sensor information. Among the balance controllers, the zero moment point (ZMP) and vibration reduction controllers were designed as state space forms where the gains could be easily changed for variable passenger weights. The stabilization performances of each controller for the variable weights were determined by comparing them with that of the previous non-adaptive controller. In Sect. 5, the performances of the walking experiments are described. The experiments verify that the walking performance of the proposed method is well maintained and superior to those of the non-adaptive controllers for three different payload levels (20 kgf, 40 kgf, and 60 kgf).

2 Hardware of the passenger-carrying biped robot, HUBO FX-1

The HUBO FX-1 is a biped robot that is capable of carrying a human and it can be operated using a joystick. The HUBO FX-1 is composed of two main parts: a lower body for locomotion and a cockpit for the passenger (Fig. 1). Harmonic reduction gears and AC servo motors with high capacities were used as actuators. The main computer, interface board, and motor drivers used to control the HUBO FX-1 are located in the cockpit. Figure 2 shows the dimensions and configuration of the joint structure. The maximum height is 1.987 mm; however, the HUBO FX-1 lowers its height by 60 mm during walking. Each leg has six degrees of freedom; hence there are 12 degrees of freedom in total.

Fig. 1 Passenger-carrying biped robot HUBO FX-1

For this type of robot, both the passenger weight and the weight of the robot itself need to be considered. Therefore, it was important to reduce the weight of the HUBO FX-1 in order to increase the payload capacity. The frame thickness of the HUBO FX-1 is approximately 12 mm, which is relatively thin, and there is no internal battery, which reduces the weight. The weight, with the exception of the external covers and the cockpit, is 130 kgf. With the external covers and cockpit, the total weight becomes 180 kgf. Assuming that the maximum payload is 100 kgf, the maximum total weight is then 280 kgf. Among the joint actuators of the HUBO FX-1, the knee joint actuator undergoes the highest torque. The maximum momentary torque at the knee joint is approximately 544 Nm if we assume that a moment arm between the knee joint and mass center is approximately 0.165 m on average, and that the safety factor for the inertial force effect is 1.2. Accordingly, the harmonic reduction gear of the CSF-32-100-2UH was used for the knee joint. This gear has a maximum momentary torque and a reduction ratio of 647 Nm and 1/100, respectively. In addition, the AC servo motor, whose maximum output torque and power are 7.644 Nm and 800 watts, respectively, was used together with the harmonic reduction gear to produce a maximum torque of 764.4 Nm at the knee joints. In this manner, all of the actuators were used in order to compensate for a passenger weight of 100 kgf. Table 1 shows the actuator specifications for the HUBO FX-1.

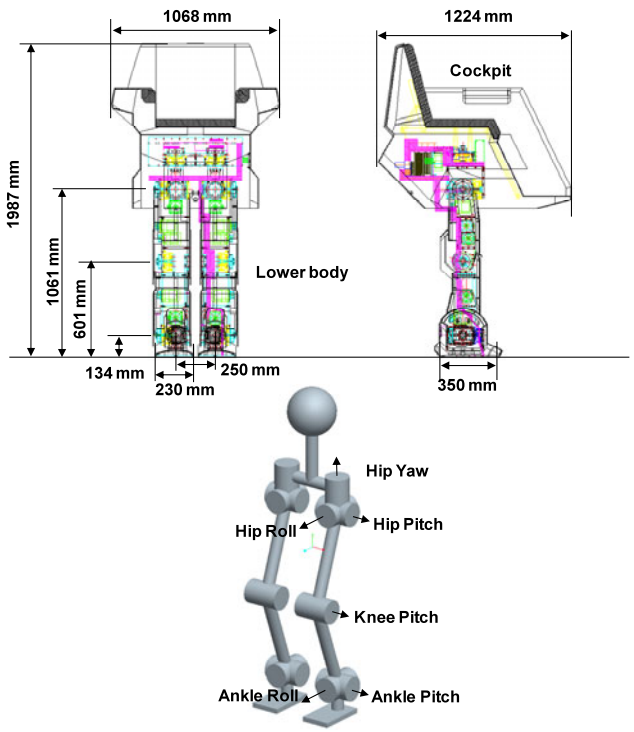

Fig. 2 Dimensions and joint structures of the robot

Three types of sensors were developed and installed in the HUBO FX-1. The first is the three-axis force/torque sensors, located on the feet, that measures the vertical ground reaction force (up to 3000 N) and the pitching and rolling ground reaction torques (up to 320 Nm). The second sensor is the inertial sensor at the pelvis center, which is composed of three rate gyros in the roll, pich and yaw directions and two accelerometers in the longitudinal (x) and lateral (y) directions. The third sensor is the accelerometer at the feet, used for the vibration control of the swing leg. With these three types of sensors and AC servo motor controllers, we built a distributed control system. If a main computer sends the desired angular positions of all of the joints to an interface card stacked on the main computer, the interface card then convert the desired angular positions into pulses and subsequently transmit them to all of the motor controllers at a frequency of 100 Hz. The sensor data can also be received at the same frequency.

3 Walking pattern generation using the convolution sum

Basically, there are no significant differences between the walking pattern generation method required in a passenger-carrying biped robot and the method required in a general biped humanoid robot. However, in a passenger-carrying walking humanoid robot, it is preferable to use a walking

Table 1 Actuator specifications

AC servo motor	400 watt	Max. torque	3.82 Nm	Applied Joints:
		Max. RPM	5000 rpm	hip pitch/yaw
				ankle pitch/roll
	800 watt	Max. torque	7.64 Nm	Applied Joints:
		Max. RPM	5000 rpm	hip roll, knee pitch
Harmonic gear	CSF-25	Reduction ratio	100:1	Applied Joints:
		Max. momentary torque	284 Nm	ankle pitch/roll
	CSF-32	Reduction ratio	100:1	Applied Joints:
		Max. momentary torque	647 Nm	hip roll/pitch/yaw
				knee pitch

pattern generation method that can accommodate variable passenger weights. Among the many walking pattern generation methods, the method using the convolution sum (proposed in the reference Kim 2007) does not require much computation power to calculate the walking patterns for variable passenger weights. This is due to the fact that the basic function required in walking pattern generation is analytically expressed in terms of the equivalent length l. This walking pattern generation method is suitable for variable passenger weights because of the characteristics of its equation, such as accuracy, low computation power and simplicity. These advantages were verified using a simulation in previous research (Kim 2007). In our previous paper on the HUBO FX-1 (Kim et al. 2007), we used the modifiable sine function for easy manual tuning of the parameters, rather than the walking pattern generation method, and we didn't solve the inverse problem between the desired ZMP and the walking pattern. The parameters of the modifiable sine patterns were obtained using a trial and error method while activating the online controllers on the robot. The walking parameters in the lateral direction were initially tuned by walking in place; subsequently, the walking parameters in the forward direction were obtained by performing forward walking. Through this manual tuning of the walking parameters, the walking performance was achieved for the specific passenger weight at which the parameters were tuned. However, the walking performance decreased if the passenger weight increased or decreased by a substantial amount. In order to maintain the walking performance in this case, it was necessary to perform exhaustive parameter tuning for the entire range of variable weights by trial and error. That was the fatal weakness in the walking pattern generation method used in previous research on the HUBO FX-1. Therefore, the effective walking pattern generation method using the convolution sum was selected for use in this research, as this method enables the easy and accurate calculation of the walking patterns for variable passenger weights and does not require much computation power.

3.1 Walking pattern generation algorithm using the convolution sum

In the walking pattern generation algorithm using convolution sum (Kim 2007), a single mass inverted pendulum model is used for a biped walking model. In this model, the ZMP equation is described by a decoupled linear differential equation in the forward and lateral directions (Kim 2007; Kajita et al. 2003; Nagasaka et al. 1999).

$$y_{ZMP} = y - \frac{1}{\lambda^2}\ddot{y} \quad \text{where } \lambda = \sqrt{\frac{g}{l}} > 0 \tag{1}$$

where g is the gravitational acceleration, l is the equivalent length of the pendulum, y is the walking pattern (i.e., displacement) of the mass center in the lateral direction, and y_{ZMP} is the reference ZMP in the lateral direction, respectively. The y-axis can be replaced by the x-axis when calculating the forward direction. When the equation of motion is expressed as (1), the trajectory of the center of mass to achieve the desired ZMP trajectory can be calculated by taking the convolution sum with it and the walking pattern for an impulse reference ZMP.

$$y[n] = \sum_{k=-\infty}^{k=\infty} u[n-k]h[k] \tag{2}$$

where, $y[k]$ is the walking pattern of the mass center in the lateral direction, $u[k]$ is an arbitrary reference ZMP input in the same axis, and $h[k]$ is the walking pattern for an impulse reference ZMP. This method is similar to the calculation of a linear system response, where the response is calculated by taking the convolution integral of the impulse response and an excitation input. Contrary to the general physical system response, the a causal relationship between center of mass and ZMP is considered to solve the inverse problem. Since the biped robot is modeled as a single inverted pendulum and its equation of motion is given by a linear differential equation, the principle of superposition can be applied and the convolution sum can be used. In this method, it is only necessary to know the walking pattern solution of the ZMP equation for the impulse reference ZMP in order to calculate the trajectory that tracks an arbitrary reference ZMP. The analytic walking pattern for an impulse reference ZMP input when the impulse reference ZMP is given at $n = 0$, was derived in the previous work (Kim 2007), and the convergent solution was solved in the discrete domain as follows:

$$h[n] = h[0] \cdot e^{-|n|\lambda T}$$
$$\text{where } h[0] = \frac{1}{2}(e^{\lambda T} - 1)e^{-\frac{\lambda T}{2}} = \sinh\left(\frac{\lambda T}{2}\right) \tag{3}$$

Figure 3 shows the plot of $h(t)$ when the impulse reference ZMP is given at $t = 0$. As seen in this figure, it is remarkable that the walking pattern occurs before the impulse reference ZMP. Since there exist walking patterns before and after the occurrence of the impulse ZMP, the solution to a given ZMP problem is not causal. However, the convolution sum in (3) is, fortunately, not divergent, since the summation of the impulse walking pattern over the time axis (i.e., the area below the function $h(t)$ in Fig. 3) is a finite value. Symmetry is also a property of $h[k]$ as seen in Fig. 3, since $h[k]$ is equal to $h[-k]$ in (3).

The walking pattern in (2) can be divided into future term and past term.

$$y[n] = y_{past}[n] + y_{future}[n]$$
$$\text{where } y_{past}[n] = \sum_{k=1}^{k=\infty} u[n-k]h[k] \tag{4}$$

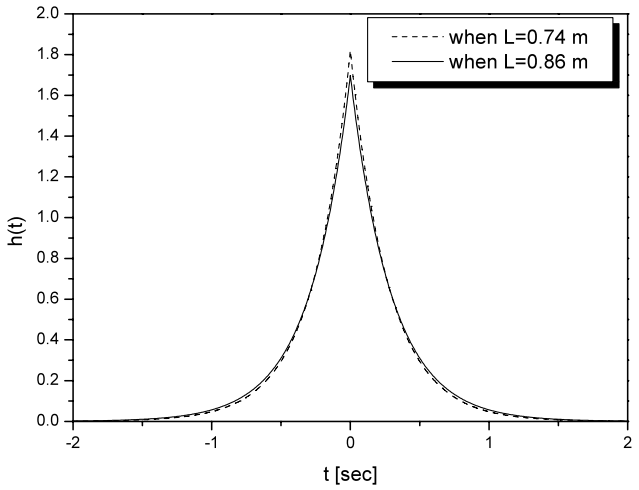

Fig. 3 Non-causal analytic walking pattern $h(t)$ for an impulse response ZMP

$$y_{future}[n] = \sum_{k=0}^{k=\infty} u[n+k]h[k] \approx \sum_{k=0}^{k=N} u[n+k]h[k] \tag{5}$$

In (5), the infinite weighted sum of $u[k]$ could be approximated using a sufficiently large number N for the weighted sum; however, this required sacrificing the accuracy. If N is large, the resultant ZMP is accurate, but it requires more computation power.

For the past term, the recursive form was derived as follows (Kim 2007):

$$y_{past}[n] = e^{-\lambda T} y_{past}[n-1] + h[1] \cdot u[n-1]$$
$$\text{where } h[1] = \sinh\left(\frac{\lambda T}{2}\right) \cdot e^{-\lambda T},\ \lambda = \sqrt{g/l} \tag{6}$$

The recursive form of the past term reduces the computation power during the process of walking pattern generation.

The online walking pattern that tracks the arbitrary reference ZMP input $u[k]$ can easily be calculated using (4), (5) and (6). This paper shows its first application in a real biped robot. The proposed algorithm has a similarity with the preview control (Kajita et al. 2003), which needs a finite future reference, but the algorithm using convolution sum does not require solving the Riccati equation to decide the preview gain and feedback gain. Specifically, the algorithm using convolution sum is suitable as a walking pattern generation method for variable passenger weights in terms of simplicity and computational load. This is due to the fact that the weighting function $h[k]$ of the future term in (5) is analytically given in terms of l, and the past term is calculated recursively in (6) so as to reduce the computational load.

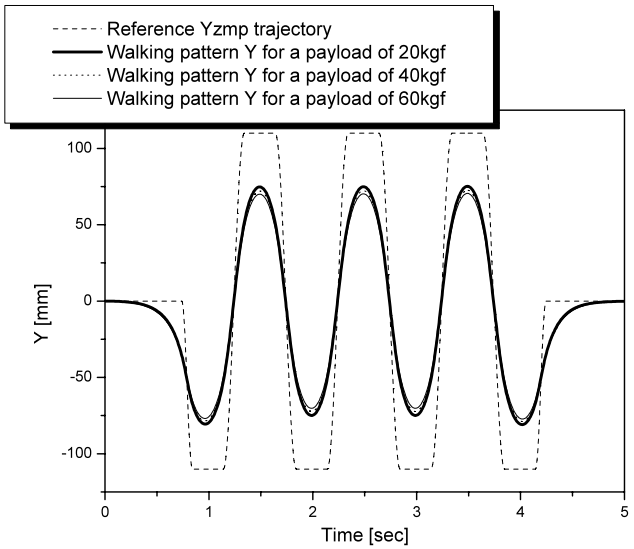

Fig. 4 Reference y_{ZMP} and walking patterns (Center of Mass) in y-direction for variable passenger weights

3.2 Walking pattern generation

This section describes the generation of walking patterns for the variable passenger weights using the convolution sum method described in Sect. 3.1. The equivalent lengths for the passenger weights of 20 kgf, 40 kgf, and 60 kgf are 0.7345 m, 0.7995 m, and 0.8538 m, respectively (the calculations of the equivalent lengths will be explained in Sect. 4.1). The walking patterns for the impulse reference ZMP, $h[k]$, are obtained using (3) and are a function of the equivalent length. The final walking patterns which tracks the reference ZMP $u[k]$ are calculated by taking the convolution sum with $h[k]$ and $u[k]$, using (4), (5) and (6). When three different levels of passenger weights (20 kgf, 40 kgf, and 60 kgf) are applied, the distinct walking patterns for the same reference ZMP along the axes y and x can be plotted (Figs. 4 and 5). The step time in these figures is 1 second, and the maximum stride is 250 mm. As seen in Fig. 4, the maximum amplitude of the hip sway for a passenger weight of 20 kgf is 80.55 mm, and it decreases as the passenger weight increases. For a passenger weight of 60 kgf, the maximum value becomes 76.83 mm. As the reference x_{ZMP} increases along the forward direction x in Fig. 5, the differences in the hip patterns along the x axis remains under the maximum of 3.5 mm. This value is relatively small compared with the maximum deviation of the hip patterns in the lateral direction y. Prescribed walking patterns for the foot are also shown in Fig. 6.

4 Balance controllers

In this section, we introduce the four types of balance controllers that we designed in order to compensate for the per-

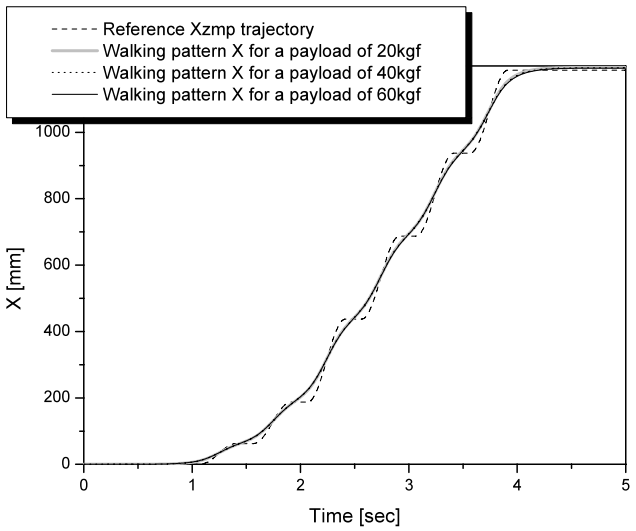

Fig. 5 Reference x_{ZMP} and walking patterns (Center of Mass) in x-direction for variable passenger weights

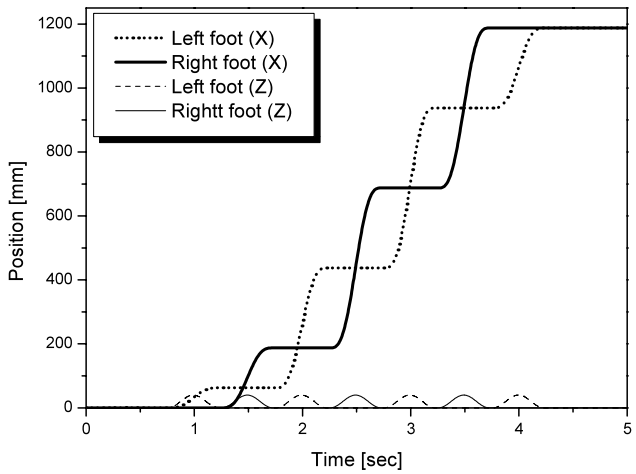

Fig. 6 Prescribed trajectories of the foot position

formance limit of the proposed walking pattern. This limit stems from the differences between an actual robot and a simplified inverted pendulum model. These balance controllers were designed in consideration of the variable passenger weights. The balance controllers introduced in previous research (Kim et al. 2007) did not consider a variable mass. However, the balance controllers proposed here are able to maintain the same balance performance in spite of variable passenger weights. The passenger weight can be easily measured by using the force/torque sensors at the feet. The balance control is based on the sensor feedback from the inertial sensor at the pelvis center and the force/torque sensors and accelerometers at the feet.

Fig. 7 Single inverted pendulum model with a flexible joint

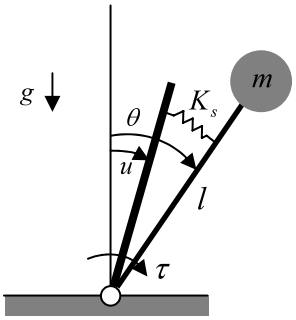

4.1 Adaptive ZMP controller

Our previous ZMP controller had a single compensator form which was composed of a state feedback controller and an observer. However, the proposed ZMP controller is based on the simple state feedback using a direct state measurement for a fast response and easy gain switching according to passenger weight. The dynamic model of the ZMP controller is a single inverted pendulum with a flexible joint (Fig. 7). Its linearized equation of motion can be represented as follows:

$$\begin{aligned} ml^2\ddot{\theta} &= mgl\theta + \tau, \\ \tau &= -K_s(\theta - u) \end{aligned} \tag{7}$$

where K_s is the torsional spring constant, l is the equivalent length, g is the gravitational acceleration, m is the point mass, and u and θ are the reference and actual angular positions of the joint, respectively. The torsional spring constant K_s represents the flexibility of the frame structure and the compliance of the ankle joint, so an actual biped robot oscillates back and forth or side to side when it is pushed and released backward or sideways during the single or double support phases. Here, it is important to note that K_s has no relation to passenger weight, whereas l and m are variable according to passenger weight. This means that the parameters of the equation of motion can change; hence, the control gain should be also changed according to the passenger weight in order to maintain the control performance.

Our previous ZMP controller assumed that l and m were constant and conducted the ZMP tracking via a state feedback controller with state variables θ and $\dot{\theta}$. These state variables were not directly measured, but were estimated from a state observer. Hence, we used a compensator by combining the state feedback controller and the observer (Fig. 8(a)). Here, y_{ZMP}^{Ref} and y_{ZMP} are the reference ZMP and the actual ZMP, respectively, and k_{ff} is the feedforward gain for the tracking control. A problem was that it was difficult to design the compensator as a function of m, l, and the closed loop poles in order to change the state feedback and observer gains according to the variable passenger weights. Therefore, in this paper, we removed the state observer and

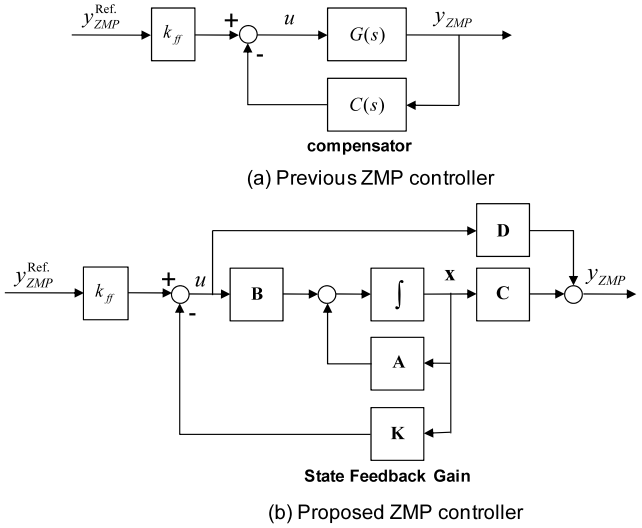

Fig. 8 Block diagrams of the previous and proposed ZMP controls

directly measured the state variables using the inertial sensor (Fig. 8(b)). In Fig. 8(b), **A**, **B**, **C** and **D** are the state, input, output, and direct transmission matrices, respectively. As such, it became possible to much more simply express the state feedback gains as a function of m, l, and the closed loop poles.

In (7), the point mass m could be measured by the force/torque sensors at the feet, and the equivalent length l could be easily calculated using the following relationships:

$$l = \frac{l_R m_R + l_P m_P}{m_R + m_P} \tag{8}$$

$$m = m_R + m_p \tag{9}$$

where m_R and m_P represent the masses of the robot (=180 kg) and the passenger, respectively, and l_R and l_P are the equivalent lengths of the robot and its passenger. The mass of the passenger m_P can be easily calculated by subtracting the weight of the robot from the total weight, and the equivalent length of the passenger l_P was assumed to be 1.45 m, which was simply calculated by considering the height of the seat and the upper body of the passenger. On the other hand, the equivalent length of the robot l_R and the torsional spring constant K_s must be calculated simultaneously through experiments. In particular, the equivalent length of the robot l_R differs depending on the single and double support phases, and the torsional spring constant K_s can also differ depending on the single and double support phase and coronal and sagittal planes. Two types of l_R and four types of K_s are shown in Fig. 9.

In (7), if we define the input, output, and state variables as the reference horizontal displacement y_r $(= lu)$, the zero moment point y_{ZMP} $(= \tau/mg)$, and the angular position θ and velocity $\dot{\theta}$, respectively, then the state space equations

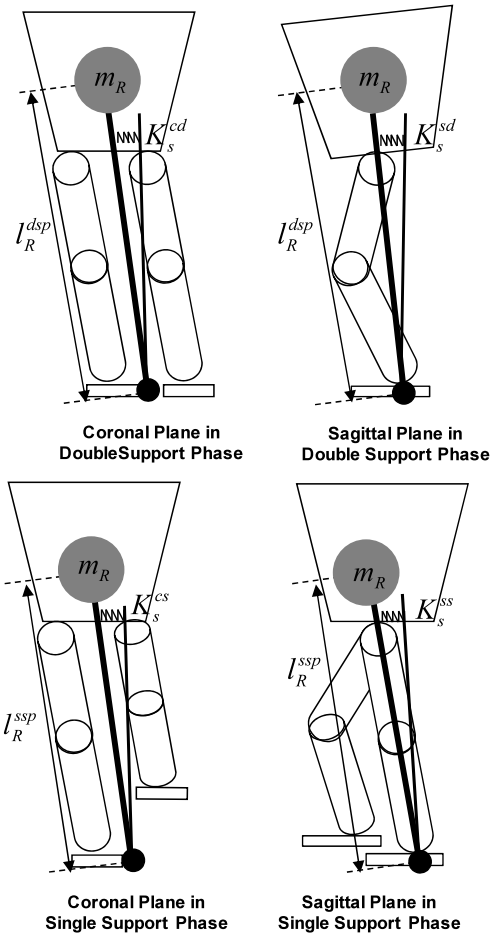

Fig. 9 Two types of l_R and four types of K_s

and transfer function $G(s)$ can be represented as follows:

$$\dot{\mathbf{x}} = \mathbf{A}\mathbf{x} + \mathbf{B}y_r$$
$$y_{ZMP} = \mathbf{C}\mathbf{x} + \mathbf{D}y_r$$
$$\text{where, } \mathbf{A} = \begin{bmatrix} 0 & 1 \\ \frac{g}{l} - \frac{K_s}{ml^2} & 0 \end{bmatrix}, \ \mathbf{B} = \begin{bmatrix} 0 \\ \frac{K_s}{ml^3} \end{bmatrix}, \tag{10}$$
$$\mathbf{C} = \begin{bmatrix} \frac{K_s}{mg} & 0 \end{bmatrix}, \ \mathbf{D} = \begin{bmatrix} -\frac{K_s}{mgl} \end{bmatrix}, \text{ and } \mathbf{x} = \begin{bmatrix} \theta \\ \dot{\theta} \end{bmatrix},$$

$$G(s) = \frac{y_{ZMP}}{y_r} = -\frac{K_s}{mgl} \cdot \frac{s^2 - \frac{g}{l}}{s^2 + \frac{K_s}{ml^2} - \frac{g}{l}} \tag{11}$$

Using (11), it is possible to calculate the two types of equivalent lengths of robot l_R and the four types of spring constant K_s by experimentally measuring the DC gain of a step response and the natural frequency without a passenger. The following (12) and (13) show the natural frequency and DC gain derived from (11). Because there is no passenger, the equivalent length l and point mass m are equal to l_R and m_R, respectively. Here, if the natural frequency ω_n and steady-state value of y_{ZMP} are experimentally measured, the

Table 2 Experimental identification of the equivalent lengths and torsional spring constants for the four cases

	Coronal plane	Sagittal plane
Double Support Phase (DSP)	$l_R^{dsp} = 0.7174$ [m] $K_s^{cd} = 21998.64$ [Nm/rad]	$l_R^{dsp} = 0.7174$ [m] $K_s^{sd} = 14784.82$ [Nm/rad]
Single Support Phase (SSP)	$l_R^{ssp} = 0.655$ [m] $K_s^{cs} = 4557.15$ [Nm/rad]	$l_R^{ssp} = 0.655$ [m] $K_s^{ss} = 5774.453$ [Nm/rad]

equivalent length of the robot l_R and the torsional spring constant K_s can be derived simultaneously.

$$\omega_n = \sqrt{\frac{K_s}{m_R l_R^2} - \frac{g}{l_R}} \tag{12}$$

$$y_{ZMP}(\infty) = \lim_{s\to 0} G(s) = \frac{K_s g}{m_R g l_R^2 \omega_n^2} \tag{13}$$

For each of the four cases in Fig. 9, we conducted experiments and then identified the equivalent lengths of the robot l_R and the torsional spring constant K_s of the HUBO FX-1 (Table 2). The spring constant was the highest for the coronal plane in the double support phase, because the supporting width was the longest. Conversely, it was the lowest for the coronal plane in the single support phase, due to the fact that it had the shortest supporting width. The equivalent lengths of the robot for the coronal and sagittal planes in each support phase were almost identical.

With the equivalent lengths and torsional spring constants for each case established, a ZMP controller based on the state feedback in each case could be proposed:

$$y_r = -\mathbf{K}\mathbf{x} \quad \text{where } \mathbf{K} = \begin{bmatrix} k_1 & k_2 \end{bmatrix} \tag{14}$$

Then, a characteristic equation was derived:

$$|s\mathbf{I} - \mathbf{A} + \mathbf{B}\mathbf{K}| = s^2 + \left(\frac{K_s}{ml^3}k_2\right)s - \frac{g}{l} + \frac{K_s}{ml^2}\left(1 + \frac{k_1}{l}\right) = 0 \tag{15}$$

If the desired closed poles are defined as $s = -a \pm bj$ $(a > 0)$ to conduct the pole placement, the state feedback gain matrix $\mathbf{K}$ becomes

$$\mathbf{K} = \begin{bmatrix} k_1 \\ k_2 \end{bmatrix} = \begin{bmatrix} \frac{[(a^2+b^2)+\frac{g}{l}]ml^3}{K_s} - l \\ \frac{2aml^3}{K_s} \end{bmatrix} \tag{16}$$

Therefore, the state feedback gain matrix can be represented as a function of m, K_s, l and the desired closed-loop poles. Since the parameters l, m, and K_s can be calculated from (8), (9) and Table 2, it is easy to change the state feedback gain according to the passenger weight. Consequently, the four types of the state feedback gain matrix are designed straightforwardly. To verify the performance of the ZMP controller, we conducted experiments with the HUBO FX-1. The closed-loop pole locations of the four cases were defined as $s = -3 \pm 3j$ by considering the suitable settling time of 1 second and a damping ratio of 0.707 in a typical second-order system. We fully pushed and released the robot to create an external disturbance and then collected the ZMP data. The external disturbances were applied to the robot in both the double and single support phases. Figures 10(a), (b), (c), and (d) show the experimental results. In each graph, we compared the four cases. The black lines in the figures represent the results without the ZMP control and a payload. Without the ZMP control, the ZMP oscillations were sustained for a long time. The red dashed lines show the results when the non-adaptive ZMP control was applied to the robot with no payload. Since there was no payload, the ZMP oscillations were effectively reduced by the non-adaptive ZMP control. However, when a large payload was applied to the robot in the presence of the non-adaptive ZMP control, the amplitudes of the ZMP oscillations increased and the settling times became longer (see blue dotted lines). Next, when we applied the adaptive ZMP control in the presence of a large payload, the amplitudes of the ZMP oscillations, described by the thick green lines decreased and the setting times became shorter compared to the results of the non-adaptive ZMP control. It is understood that the ZMP oscillations were reduced much faster with the adaptive ZMP control. Consequently, the settling times for all cases are summarized in Tables 3 and 4. As seen in Tables, the settling time with the non-adaptive ZMP control increased according to the payload, while the adaptive ZMP control maintained a short settling time of approximately 2 seconds regardless of the payload. Therefore, the adaptive ZMP control clearly showed a superior performance to the non-adaptive ZMP control used in our previous research.

The walking pattern was divided into eight stages in order to effectively apply the ZMP controller to the robot during the actual walking process (Fig. 11). The criteria for dividing the walking stages were the points of time when a biped robot starts to lift and lower the swing foot and when the vertical ground reaction force on the swing foot starts to exceed the predefined contact threshold. The zero stage is the double support phase between the walking start and lifting the left swing foot. The first stage is the single support phase

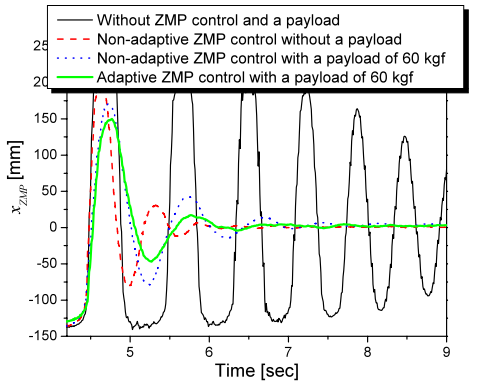

(a) x_{ZMP} in the double support phase

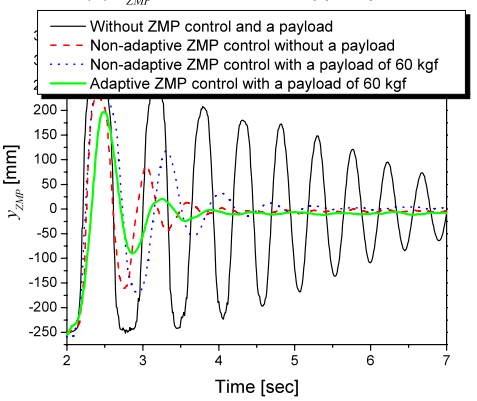

(b) y_{ZMP} in the double support phase

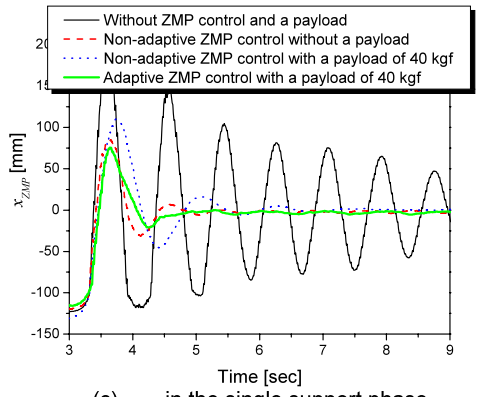

(c) x_{ZMP} in the single support phase

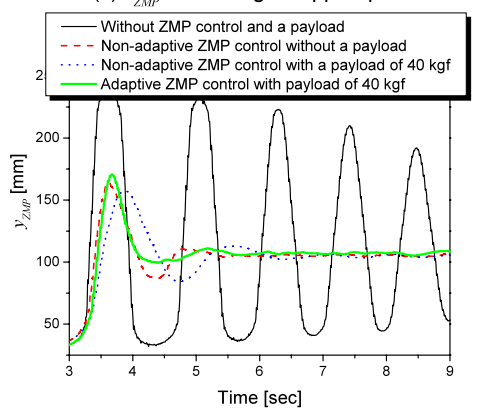

(d) y_{ZMP} in the single support phase

Fig. 10 Experimental results of ZMP control with payloads

from the point when the left swing foot has started to lift until the time when the left swing foot starts to lower. The second stage is the single support phase from the time when the left swing foot starts to lower until its first contact with the ground. The third stage is the double support phase from the start of the double foot contact until the right swing foot begins to lift. The fourth to sixth stages are determined using the same procedures as described, but for the right foot. The seventh stage contains the mixed phases from when the swing foot begins to lower until the start of the next footstep. The first through sixth stages are repeated during the walking process.

We determined the stages in which the DSP (double support phase) ZMP controller or SSP (single support phase) ZMP controller should be applied:

(1) stages where DSP ZMP control is applied: 0 and seventh stages
(2) stages where SSP ZMP control is applied: first through sixth stages

The double support phase exists between the first and sixth stages. For a human, the double support ratio is approximately 20% during a normal walking cycle, because a human uses toe joints which increase the double support ratio. However, the HUBO FX-1 does not have toe joints; therefore, the double support ratio is only 5%. Because of this, we did not use the DSP ZMP controller during very short periods between the first and sixth stages. For the controller switching, the final gains were introduced (Fig. 12). Since the control inputs were multiplied by the final gains that smoothly change between 0 and 1, it was possible to switch the DSP and SSP ZMP controllers without a jerk.

4.2 Adaptive landing timing controller

Though the walking pattern and the ZMP controller of a biped robot are designed well, actual biped walking of the robot does not completely coincide with the designed walking pattern due to the unmodeled dynamics, uneven ground and various disturbances. A basic strategy for solving this problem is the modification of the walking pattern according to the ground contact time. The ground contact times of both feet are predefined in a given walking pattern. However, the actual ground contact may happen earlier or later than the predefined time. If the walking pattern is not modified by considering the actual ground contact time, a robust walking performance cannot be achieved. In order to solve this problem, we divided the ground contact into an early landing case and a late landing case. A difficulty involved in this was determining the ground contact time.

In our previous research (Kim et al. 2007), we assumed that the foot is in contact with the ground when a vertical ground reaction force higher than 5 kgf was measured on the

Table 3 Approximate settling time in the double support phase

	Non-adaptive ZMP control without a payload	Non-adaptive ZMP control with a payload of 30 kgf	Non-adaptive ZMP control with a payload of 60 kgf	Adaptive ZMP control with a payload of 30 kgf	Adaptive ZMP control with a payload of 60 kgf
Settling time of x_{ZMP} control in DSP	1.9 [sec]	2.4 [sec]	2.9 [sec]	1.8 [sec]	1.9 [sec]
Settling time of y_{ZMP} control in DSP	2.1 [sec]	2.9 [sec]	3.4 [sec]	2.0 [sec]	2.1 [sec]

Table 4 Approximate settling time in the single support phase

	Non-adaptive ZMP control without a payload	Non-adaptive ZMP control with a payload of 20 kgf	Non-adaptive ZMP control with a payload of 40 kgf	Adaptive ZMP control with a payload of 20 kgf	Adaptive ZMP control with a payload of 40 kgf
Settling time of x_{ZMP} control in SSP	2.2 [sec]	2.9 [sec]	3.6 [sec]	2.1 [sec]	2.1 [sec]
Settling time of y_{ZMP} control in SSP	2.4 [sec]	3.1 [sec]	3.9 [sec]	2.5 [sec]	2.6 [sec]

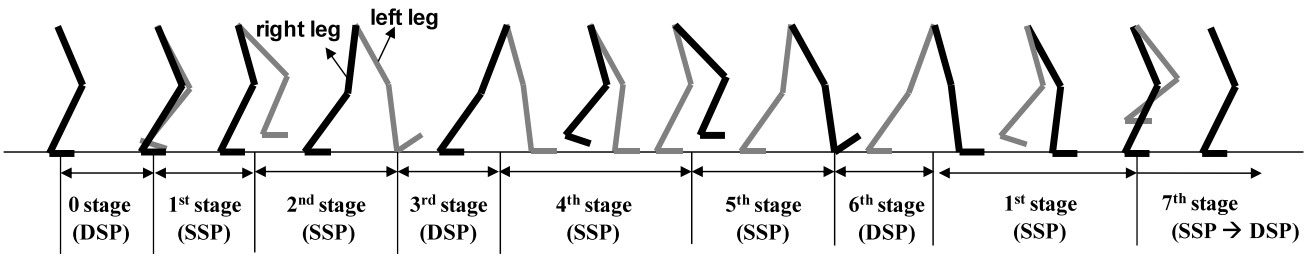

Fig. 11 Walking stages

Fig. 12 Final gains of ZMP control

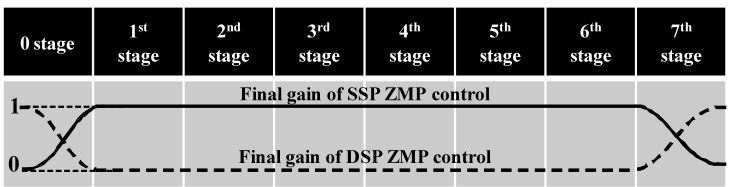

foot force sensor for a biped humanoid robot with a weight of 60 kgf. However, in this research, as the passenger weight is not constant, the contact threshold should be proportionally defined according to the total weight. Consequently, the contact threshold was defined as 8% of the total weight, as would follow with a contact threshold of 5 kgf for a 60 kgf robot.

The contact threshold is closely related to the walking stages. The second, third, fifth, and sixth stages are the period in which the swing foot lowers. Here, a criterion that distinguishes between the second and third stages and the fifth and sixth stages becomes the contact threshold. For example, the second stage becomes longer and the third stage becomes shorter for a late landing case. Conversely, the second stage shortens and the third stage lengthens for an early landing case. The landing timing controller is utilized during the second and third stages or during the fifth and sixth stages. Its control strategy is described as follows:

(1) *Late landing case*: if the vertical ground force is not applied to the swing foot when the swing foot has been lowered to the prescribed position, then it delays the start of the fourth or first stage until the vertical

ground reaction force exceeds the contact threshold (see Fig. 13).

(2) *Early landing case*: if the vertical ground force on the swing foot already exceeds the contact threshold, 8% of the total weight, before the swing foot has been lowered to the prescribed position, then it waits to lower the swing foot so as to prevent the swing foot from strongly contacting the ground. Then, it lowers the swing foot to the prescribed position smoothly during the fourth or first stage (see Fig. 13).

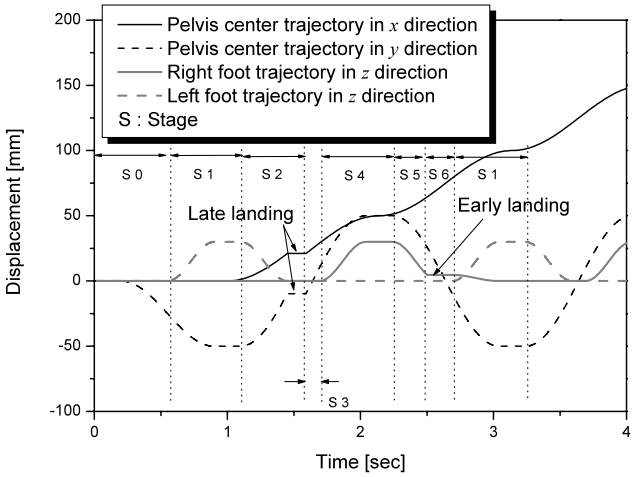

Fig. 13 Schematics of the adaptive landing timing control

4.3 Adaptive vibration reduction controller

The frame of the HUBO FX-1 was designed to be thin in order to reduce its weight and to increase its payload capacity. However, this resulted in relatively large structural vibrations during walking, which decreases the accuracy and repeatability of the landing position on the ground. The structural vibrations have three vibration modes (Fig. 14). The first and second vibration modes are the rolling and pitching vibrations of the swing leg, and the third vibration mode is the yawing vibration of the whole body with respect to the supporting leg. To solve the issues associated with the aforementioned problems, we applied a vibration reduction controller to the HUBO FX-1 in our previous research. Previously, a variation in the passenger weight was not considered for the third vibration mode, while this paper considers the variable passenger weight for it.

The swing leg of the first vibration mode was modeled as a pendulum with a flexible joint on the coronal plane. If the gravitational acceleration is ignored, an equation of motion

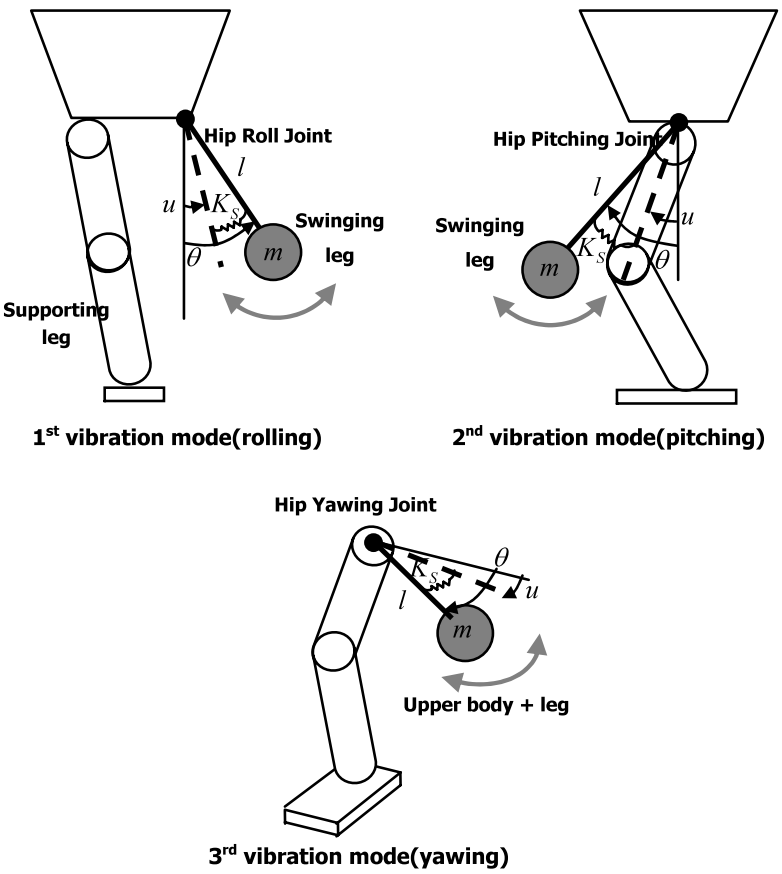

Fig. 14 Three types of vibration modes

and a transfer function can be simply derived as follows:

$$ml^2\ddot{\theta} = -K_s(\theta - u) \tag{17}$$

$$\frac{\Theta(s)}{U(s)} = \frac{K_s/ml^2}{s^2 + K_s/ml^2} \tag{18}$$

where K_s is the torsional spring constant, l is the equivalent length, m is the point mass of the leg, and u and θ are the reference and actual angular positions of the hip roll joint of the swing leg, respectively. Since the point mass of the leg is not related to the passenger weight, the equation of motion was simply identified by measuring the natural frequency $\omega_n (= \sqrt{K_s/ml^2})$ through an impulse response experiment. Next, we designed a control block diagram using a lead compensator (Fig. 15). An accelerometer on the foot was used as a feedback sensor, and the leaking integrator was used to calculate the angular position without large overshoots. This control method was also applied to the second vibration mode. Figure 16 shows the experimental results. Thus, the structural vibrations in the x and y-directions were rapidly reduced through the use of the vibration reduction controller.

Next, the upper body and the swing leg were modeled as a pendulum with a flexible joint on the transverse plane in order to design a vibration reduction controller for the third vibration mode. Since the gravitational acceleration was ignored, an equation of motion and a transfer function of this mode were used, as with (17) and (18).

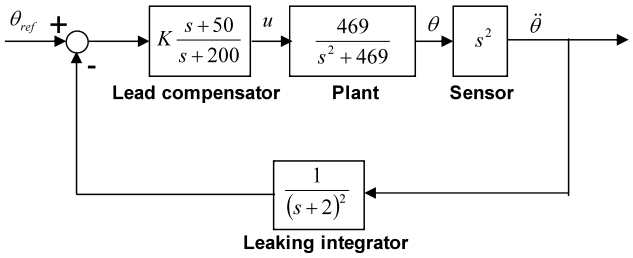

Fig. 15 Control block diagram of the first vibration mode (Kim et al. 2007)

However, at this time, u and θ are the reference and actual angular positions of the hip yaw joint of the supporting leg. Since, in this mode, the passenger weight is included in the point mass m, it significantly changes the parameters in the equation of motion. The equivalent length l is also variable; however, it is insensitive to the variable passenger weights, because the passenger weight is loaded above the pelvis center. Hence, we assumed that the equivalent length l was 0.2 m. First, the torsional spring constant K_s was derived by experimentally measuring the natural frequency without a passenger weight as follows:

$$K_s = ml^2\left(\frac{2\pi}{T}\right)^2 \tag{19}$$

As a result, the period of the vibration T was 0.36 seconds and the K_s was calculated at 1705.9 Nm/rad. Since our previous vibration controller for the third vibration mode did not consider the gain changing due to the variable passenger weights, a simple lead compensator was used at that time. However, as the variable passenger weights needed to be incorporated, we used the state space equation with a direct state feedback. To build a state space equation, the state variables were defined as the angular position θ and the angular velocity $\dot{\theta}$ at the pelvis center. Equation (20) details the state space equation, and the state feedback was designed as shown in the block diagram of Fig. 17.

$$\begin{aligned}
&\dot{\mathbf{x}} = \mathbf{A}_v\mathbf{x} + \mathbf{B}_v u \\
&y = \mathbf{C}_v\mathbf{x} \\
&\text{where, } \mathbf{A}_v = \begin{bmatrix} 0 & 1 \\ -\frac{K_s}{ml^2} & 0 \end{bmatrix},\ \mathbf{B}_v = \begin{bmatrix} 0 \\ \frac{K_s}{ml^2} \end{bmatrix}, \\
&\mathbf{C}_v = \begin{bmatrix} 1 & 0 \end{bmatrix},\quad \text{and } \mathbf{x} = \begin{bmatrix} \theta & \dot{\theta} \end{bmatrix}^T
\end{aligned} \tag{20}$$

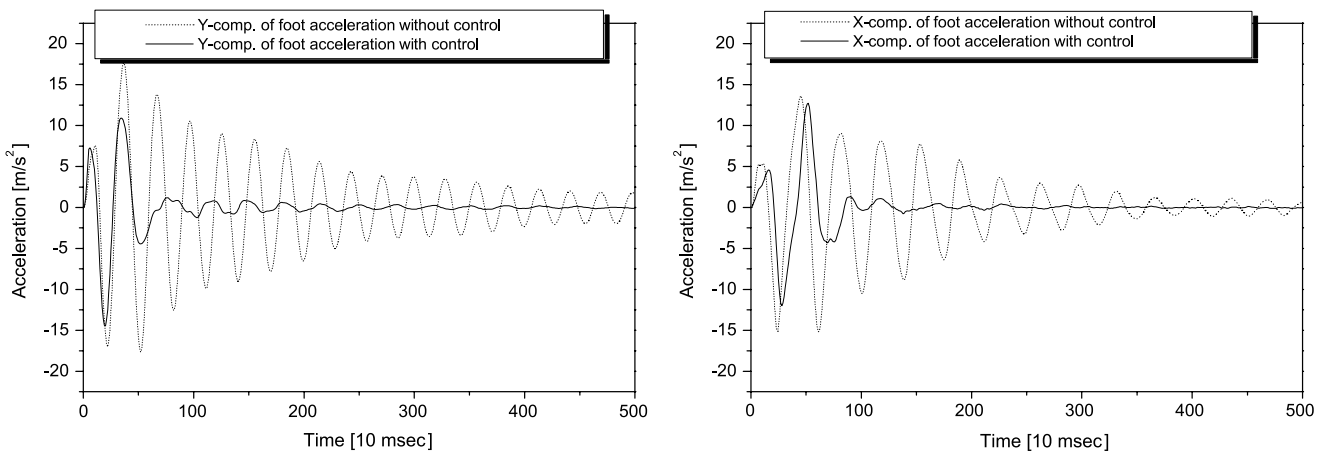

Fig. 16 Experimental results of the first and second vibration reduction controls (Kim et al. 2007)

Using the pole placement, the state feedback gain matrix $\mathbf{K}_v$ that locates the closed-loop poles on $s = -c \pm dj$ $(c > 0)$ in the S-plane was derived as follows:

$$\mathbf{K}_v = \begin{bmatrix} k_{v1} \\ k_{v2} \end{bmatrix} = \begin{bmatrix} \frac{ml^2}{K_s}(c^2 + d^2) - 1 \\ 2c \cdot \frac{ml^2}{K_s} \end{bmatrix} \tag{21}$$

The state variables were measured using a rate gyro that measures the yawing angular velocity at the pelvis center of the HUBO FX-1. The yawing angular velocity was filtered via a low-pass filter with a cut-off frequency of 10 Hz. The yawing angular position was obtained via a high-pass filter with a cut-off frequency of 0.5 Hz and an integrator. The close-loop pole was chose as $s = -4 \pm 4j$. Figure 18 shows the experimental results. Without the vibration reduction control, the yawing oscillation, shown in the figure in black, was sustained for a long time, while the oscillations shown as blue and red were rapidly reduced in 0.9 seconds with the adaptive vibration reduction control for the two different payloads. In Fig. 19, the vibration reduction controllers of all the modes were applied during the first and fourth stages in the single support phase. In addition, the control inputs were multiplied by the final gains to enable smooth starts and stops.

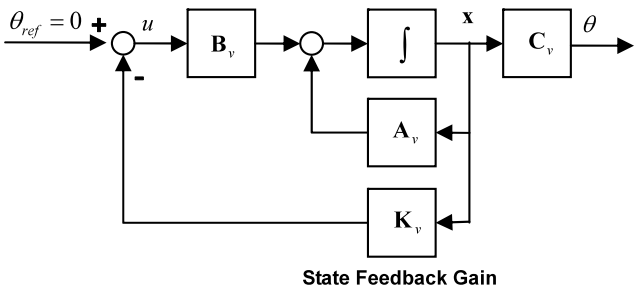

Fig. 17 Control block diagram of the third vibration mode

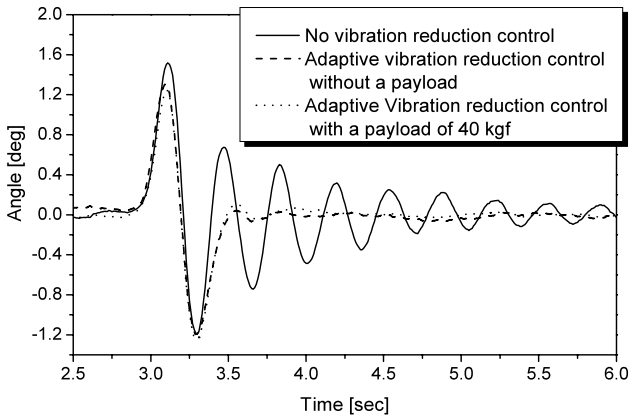

Fig. 18 Experimental results of the vibration reduction control for the third vibration mode

5 Walking experiments

In this section, we describe the walking experiments in which we illustrated the effectiveness of the proposed walking pattern generation and balance control for variable passenger weights. As the passengers of the HUBO FX-1 can be categorized into either children or adults, the walking performances were compared and analyzed with payloads of 20 kgf, 40 kgf, and 60 kgf. After the payload was loaded into the cockpit, the force/torque sensor measured the payload, and then the equivalent pendulum lengths of the single and double support phases for the ZMP control were calculated. After this, we calculated the state feedback gains of the ZMP controllers and the vibration reduction controller for the third mode, as well as the contact threshold of the landing timing controller. In addition, the walking pat-tern was generated according to the calculated equivalent pendulum length of the single support phase and the predefined ZMP reference trajectory (as outlined in Sect. 3.2). Finally, the balance control inputs were superimposed onto the generated walking pattern during walking.

The walking experiments were conducted on a normal room floor with a local slope of approximately ±2 degrees. During the walking experiments, we collected the ZMP trajectories and body inclinations so as to compare the walking performances between the non-adaptive and adaptive cases in terms of walking pattern and balance control. The walking parameters used in this experiment are as follows: step time = 1.0 second, step length = 250 mm, max. lift of the swing foot = 40 mm, and double support ratio = 5%. First, we performed walking experiments for the non-adaptive case in order to reproduce the walking performance of our previous research. Here, walking patterns and balance control gains were obtained by considering only the robot weight. Second, we also performed walking experiments with the adaptive walking pattern and adaptive balance control. The walking experiments of each case were conducted for the three different payloads. As a result, we derived Table 5. Table 5

Fig. 19 Final gains of the vibration reduction controls

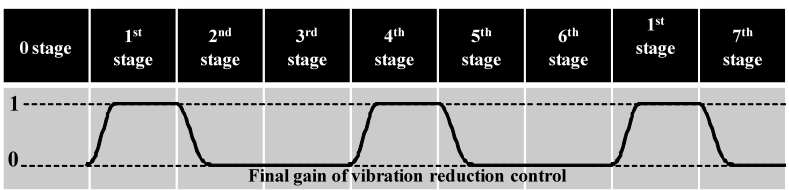

Table 5 RMS values of ZMP tracking errors and body inclinations for each case

	Payload [kgf]	RMS value of x_{ZMP} error [mm]	RMS value of y_{ZMP} error [mm]	RMS value of rolling body inclination [deg]	RMS value of pitching body inclination [deg]
Non-adaptive case	20	40.39	54.56	1.57	0.82
	40	58.85	55.12	1.06	1.0
	60	56.92	56.39	1.35	0.91
Adaptive case	20	36.79	40.55	0.6	0.83
	40	36.64	38.88	0.72	0.63
	60	46.93	36.47	0.89	0.87

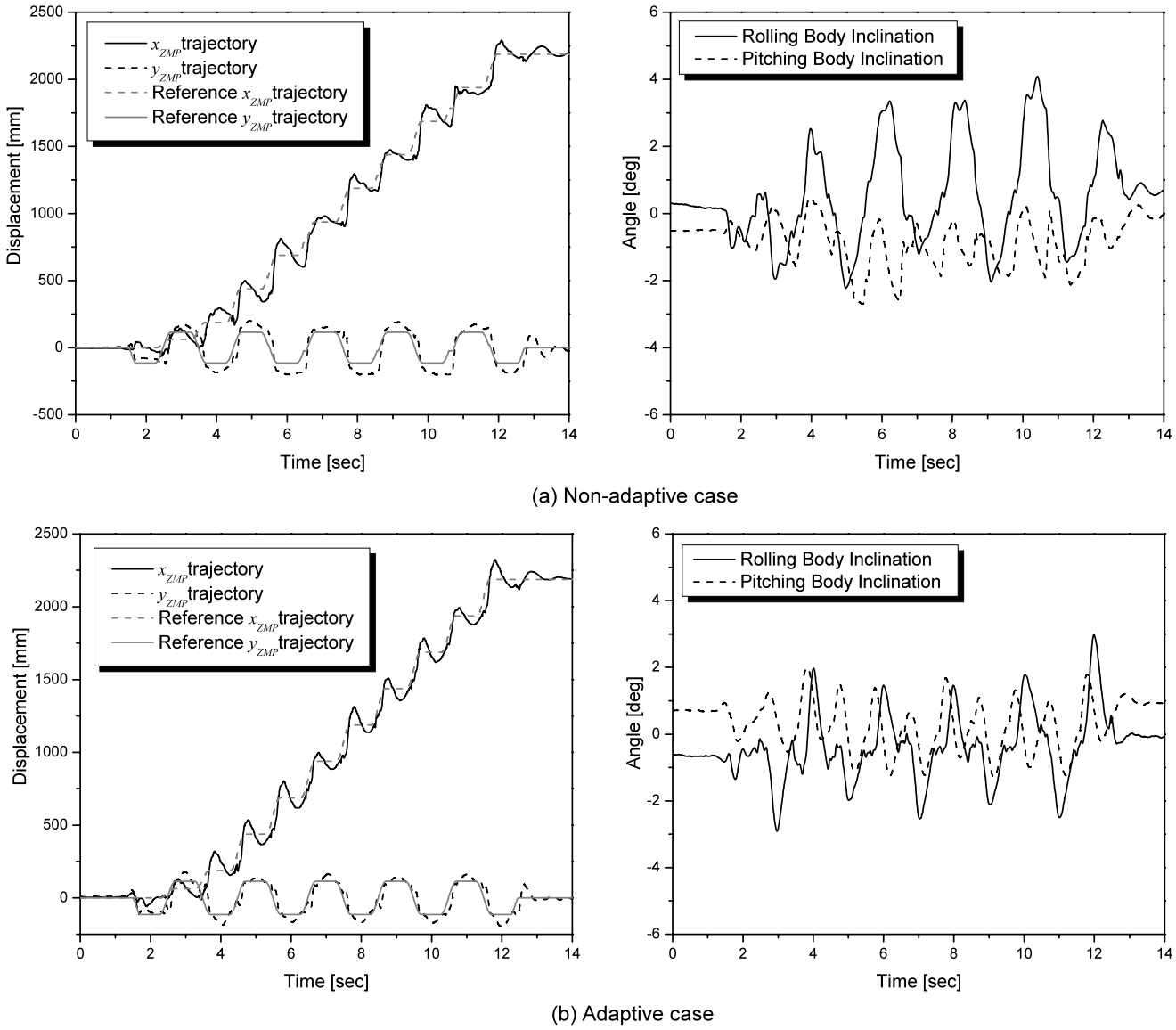

Fig. 20 Comparison of ZMP trajectories and body inclinations between non-adaptive and adaptive cases with a payload of 60 kgf

details the RMS (root mean square) values of the ZMP tracking errors and body inclinations for both cases. As shown in the table, the RMS values of the ZMP tracking errors of the non-adaptive cases generally increased as the payload increased, while the walking performances of the adaptive cases maintained their performance in spite of the payload change. Also, the RMS values of both the ZMP tracking errors and body inclinations of the adaptive case were much less than those of the non-adaptive cases. More specifically, The RMS values of the x_{ZMP} and y_{ZMP} errors for the adaptive case were reduced by approximately 23% and 30%, respectively on the average. In addition, the RMS values of the rolling and pitching body inclinations for the adaptive case were also reduced by approximately 44% and 14%, respectively on the average. For reference, Fig. 20 show the experimental results of the ZMP trajectories and the body inclinations for the payloads of 60 kgf. This figure indicate that the HUBO FX-1 walked more stably with the adaptive walking pattern and balance control. Thus, we were able to show the effectiveness of the proposed algorithm using walking experiments with the HUBO FX-1.

A final walking pattern including the balance control inputs, and a snapshot of the adaptive case with a payload of 60 kgf are represented in Figs. 21 and 22.

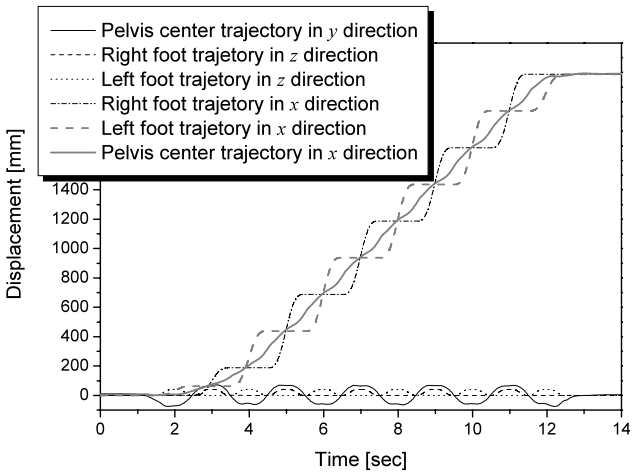

Fig. 21 Final walking pattern including balance control inputs in the adaptive case with a payload of 60 kgf

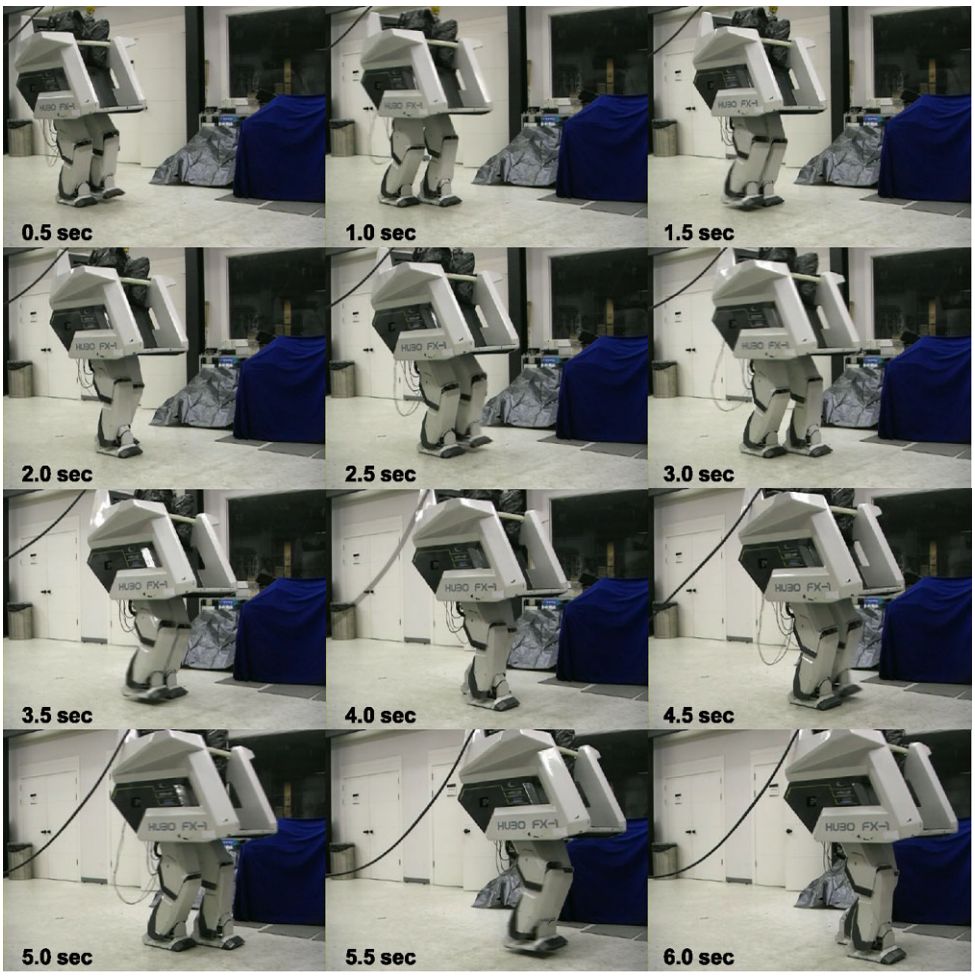

Fig. 22 Snapshot of the HUBO FX-1 forward walking with a payload of 60 kgf

6 Conclusions

This research focused on the adaptive walking pattern generation methods and balance control algorithms for the passenger-carrying biped robot, HUBO FX-1, for variable passenger weights. Our previous research on the HUBO FX-1 has several drawbacks in that the walking patterns were experimentally obtained by trial and error, and the control gains of the balance controllers were selected by considering a constant passenger weight of 81 kgf. Using our previous method, the walking performance would decrease when a passenger weighed more or less than the predefined passenger weight. In order to solve this problem, this paper proposed a method to preserve the walking performance by changing the walking pattern and control gains depending on the passenger weight. Therefore, the previous controllers such as the ZMP controller, landing time controller, and vibration reduction controller were improved through the use of the variable gains that were easily calculated after measuring the passenger weight from force/torque sensors and calculating the equivalent length l. The frameworks of the balance controllers were modified from the previous algorithm so that the following attributes were all corrected to the weight of the passenger: the state feedback gains of the ZMP controller and the vibration reduction controller, and the contact threshold. For the walking pattern generation, our method used the convolution sum. Since this method contains the analytic weighting function of the equivalent length l, it can effectively calculate the walking pattern for variable passenger weights. Finally, the walking performances in the adaptive control method and the previous non-adaptive control method were quantitatively analyzed in terms of the ZMP and inclination for various passenger weights on the HUBO FX-1. The experimental results verified that the proposed adaptive method enables a better walking performance for different passenger weights.

In the experimental results, there still existed some amount of ZMP error that led to the peaks in spite of using the adaptive control and walking pattern. We can consider the several reasons as follows:

- There are measurement errors in the force-torque sensors and the inertial sensor.
- The load is shaking a little bit during walking.
- The landing impact leads to the shaking of the robot body.
- Since we use the single inverted pendulum model, there is a fundamental modeling error.
- Since we use linear controllers, there are fundamental errors due to the linearization.
- Control gains are not perfect.

Therefore, we suggest the following three topics that should be considered to reduce the ZMP error more:

- Walking pattern generation and controller design by considering a more complex dynamic model that reflects the vertical movement of the swing foot and the horizontal movement of the passenger.
- Determination of the optimal control gains for the balance controllers.
- Control strategies for the effective impact absorption during walking.

All of these aforementioned topics for future research will be systematically studied and reported upon by our group.

Acknowledgements This research was supported by the Ministry of Knowledge and Economy (MKE), South Korea under grants No. 10035431, development of wearable robot for industrial labor support and No. F0005000-2010-32, development of biped walking control algorithm on general floors.

References

Akachi, K., Kaneko, K., Kanehira, N., Ota, S., Miyamori, G., Hirata, M. Kajita, S., & Kanehiro, F. (2005). Development of humanoid robot HRP-3P. In *Proceedings of the IEEE-RAS international conference on humanoid robots*, Tsukuba, Japan, December 2005 (pp. 50–55).

Chestnutt, J., Michel, P., Nishiwaki, K., Kuffner, J., & Kagami, S. (2006). An intelligent joystick for biped control. In *Proceedings of the IEEE international conference on robotics and automations*, Orlando, FL, May 2006 (pp. 860–865).

Gienger, M., Janssen, H., & Goerick, C. (2005). Task-oriented whole body motion for humanoid robots. In *Proceedings of the 2005 IEEE-RAS international conference on humanoid robots*, Tsukuba, Japan, December 2005 (pp. 238–244).

Hirai, K., Hirose, M., Haikawa, Y., & Takenaka, T. (1998). The development of Honda humanoid robot. In *Proceedings of the 1998 IEEE international conference on robotics and automations*, Leuven, Belgium, May 1998 (pp. 1321–1326).

Kajita, S., Kanehiro, F., Kaneko, K., Fujiwara, K., Harada, K., Yokoi, K., & Hirukawa, H. (2003). Biped walking pattern generation by using preview control of zero-moment point. In *Proceedings of the 2003 IEEE international conference on robotics and automation*, Taipei, Taiwan, September 2003 (pp. 1620–1626).

Kim, J. H. (2007). Walking pattern generation of a biped walking robot using convolution sum. In *Proceedings of the 2007 IEEE-RAS international conference on humanoid robots*, Pittsburgh, PA, November 2007 (pp. 539–544).

Kim, J. Y., Lee, J., & Oh, J. H. (2007). Experimental realization of dynamic walking for a human-riding biped robot, HUBO FX-1. *Advanced Robotics*, *21*(3), 461–484.

Löffler, K., Gienger, M., & Pfeiffer, F. (2003). Sensor and control design of a dynamically stable biped robot. In *Proceedings of the 2003 IEEE international conference on robotics and automations*, Taipei, Taiwan, September 2003 (pp. 484–490).

Nagasaka, K., Inoue, H., & Inaba, M. (1999). Dynamic walking pattern generation for a humanoid robot based on optimal gradient method. In *Proceedings of the 1999 IEEE international conference on systems, man, and cybernetics*, Tokyo, Japan, October 1999 (pp. 908–913).

Ogura, Y., Aikawa, H., Shimomura, K., Kondo, H., Morishima, A., Lim, H. O., & Takanishi, A. (2006). Development of a new humanoid robot WABIAN-2. In *Proceedings of the 2006 IEEE international conference on robotics and automations*, Orlando, FL, May 2006 (pp. 76–81).

Park, I. W., Kim, J. Y., Lee, J., & Oh, J. H. (2005). Mechanical design of humanoid robot platform KHR-3 (KAIST Humanoid Robot—3: HUBO). In *Proceedings of the 2005 IEEE-RAS international conference on humanoid robots*, Tsukuba, Japan, December 2005 (pp. 321–326).

Stilman, M., Nishiwaki, K., Kagami, S., & Kuffner, J. (2007). Planning and executing navigation among movable obstacles. *Advanced Robotics*, *21*(3), 1617–1634.

Sugahara, Y., Lim, H., Hosobata, T., Mikuriya, Y., Sunazuka, H., & Takanishi, A. (2004). Realization of dynamic human-carrying walking by a biped locomotor. In *Proceedings of the 2004 IEEE international conference on robotics and automations*, New Orleans, LA, April 2004 (pp. 3055–3060).

Toyota motor corporation (2004), Toyota.co.jp, news release, http://www.toyota.co.jp/en/news/04/1203_1d.html.

Jung-Hoon Kim received his B.S. degree in Mechanical Design and Production Engineering from Yonsei University, Seoul, South Korea and M.S. and Ph.D. degrees in Mechanical Engineering from KAIST, Daejeon, South Korea in 1997, 1999 and 2004, respectively. From 2004 to 2005, he was a Post-doctoral Researcher in the University of California, Berkeley. From 2005 to 2006, he was a Senior Engineer at Mechatronics Center in Samsung Electronics. He was an assistant professor in the Department of Mechanical Engineering, Myongji University, from 2006 to 2008. Since 2008, he has been with the Department of Civil and Environmental Engineering, Yonsei University, where he is currently an assistant professor.

Jung-Yup Kim received his B.S. and M.S. degrees in Mechanical Engineering from Inha University, Incheon, South Korea, and Ph.D. degree in Mechanical Engineering from KAIST, Daejeon, South Korea, in 1999, 2001 and 2006, respectively. He was a Post-doctoral Fellow of Humanoid Robot Research Center at KAIST and Robotics Institute of Carnegie Mellon University, Pittsburgh, USA in 2006 and 2007 respectively. Since 2008, he has been with School of Mechanical Design and Automation Engineering of Seoul National University of Science & Technology, Seoul, South Korea, where he is currently an Assistant Professor.

Jun-Ho Oh received his B.S. and M.S. degrees in Mechanical Engineering from Yonsei University, Seoul, South Korea, and Ph.D. degree in Mechanical Engineering from University of California, Berkeley, in 1977, 1979, and 1985 respectively. He was a Researcher with the Korea Atomic Energy Research Institute, from 1979 to 1981. Since 1985, he has been with the Department of Mechanical Engineering, KAIST, where he is currently a professor and a director of Humanoid Robot Research Center (HUBO Lab.).